Supplementary Information (SI) for Green Chemistry.

Upcycling Poly(ε-caprolactone) into Azepane via Reductive Ammonolysis over a Titanium Oxide-supported Platinum Catalyst

Daratu E. K. Putri,[a,b] Katsumasa Sakoda,[a] Yoshiki Takamoto,[a] Sho Yamaguchi,[a,c] Takato Mitsudome,[a,d] and Tomoo Mizugaki*[a,d,e]

*Corresponding author: mizugaki.tomoo.es@osaka-u.ac.jp

[a] Department of Materials Engineering Science, Graduate School of Engineering Science, The University of Osaka, 1-3 Machikaneyama, Toyonaka, Osaka 560-8531, Japan

[b] Departemen Kimia, Fakultas Matematika dan Ilmu Pengetahuan Alam, Universitas Negeri Malang, Jl. Semarang 5, Lowokwaru, Malang 65145, Indonesia

[c] Graduate School of Engineering, Kobe University, Kobe, Hyogo 657-8501, Japan

[d] Innovative Catalysis Science Division, Institute for Open and Transdisciplinary Research Initiatives (ICS-OTRI), The University of Osaka, Suita, Osaka 565-0871, Japan

[e] Research Center for Solar Energy Chemistry, Graduate School of Engineering Science, The University Osaka, 1-3 Machikaneyama, Toyonaka, Osaka 560-8531, Japan

Table of Content

1. General experimental details

Organic chemicals were purchased from Fujifilm Wako Pure Chemical Industries, Ltd., Tokyo Chemical Industry Co., Ltd., and Sigma-Aldrich, and were used as received. H_2PtCl_6 was obtained from N. E. Chemcat or Fujifilm Wako Pure Chemical Industries. $RuCl_3$, K_3RhCl_6, and $Pd(NH_3)_4Cl_2$ hydrates were obtained from N. E. Chemcat. TiO_2 (JRC-TIO-9) and ZrO_2 (JRC-ZRO-7) were supplied by the Catalyst Society of Japan as the reference catalyst. γ-Al_2O_3 and CeO_2 (Type-A1) were obtained from Sumitomo Chemical Co., Ltd. and Daiichi Kigenso Kagaku Kogyo Co., Ltd., respectively. Gas chromatography (GC-FID) analyses were performed on a Shimadzu GC-2014SE instrument equipped with a capillary column (InertCap for amines, GL Science, 30 m x 0.32 mm i.d.). The gel permeation chromatography (GPC) was performed using chloroform at 40 ºC with columns (KF-804L column × 2; flow rate = 1.0 mL/min) connected to a JASCO PU4180 pump, a CO4060 column oven, a UV4575 ultraviolet detector, and an RI4030 refractive-index detector. ^1H nuclear magnetic resonance (NMR) spectra were recorded using a JEOL JNM-ESC400 spectrometer. Chemical shifts are reported as follows: *s*-trioxane (5.12 ppm) as an external standard in D_2O solvent, TMS (0 ppm for ^1H-NMR) in $CDCl_3$. NMR multiplicities are reported using the following abbreviations: *s*, singlet; *d*, doublet; *t*, triplet; *q*, quartet; quint, quinted; *m*, multiplet; *br*, broad; *J*, coupling constants in hertz. Transmission electron microscopy (TEM) images were obtained using a Hitachi HF-2000 microscope instrument operating at 200 kV at the Research Center for Ultra-High Voltage Electron Microscopy (Nanotechnology Open Facilities) in The University of Osaka. Pt L_3-edge and Mo K-edge X-ray absorption near-edge structure (XANES) spectra were recorded at room temperature in transmittance mode using Si (311) monochromators at the 14B2 and 01B1 beam line stations at SPring-8, Japan Atomic Energy Research Institute (JASRI), Harima, Japan (promotion number: 2024A1548 and 2025A1813). Data analysis was performed using Demeter ver. 0.9.21. X-ray photoelectron spectroscopy (XPS) spectra of the samples were obtained using a ULVAC-PHI ESCA 3057 system, and the binding energy was referenced to the C 1s peak (285.0 eV). Inductively coupled plasma-atomic emission spectroscopy (ICP-AES) measurements was performed using a Perkin Elmer Optima 8300 instrument. CHN elemental analyses were performed using a Perkin Elmer 2400IICHNS/O. Fourier-transform infrared (FT-IR) spectra were recorded using a JASCO FT-IR 4100 spectrometer equipped with a mercury cadmium telluride detector. The NH_3-temperature programmed desorption (TPD) data was measured using a BELCAT-A instrument (BEL Japan Inc.) equipped with mass spectrometer (BELMASSII, BEL Japan Inc.).

2. Catalyst preparation and reaction procedures

Preparation of metal oxide-supported catalysts

The Pt/TiO_2 catalyst was prepared by impregnation method. Aqueous solution of H_2PtCl_6 (6.00 mL, 100 mM) and TiO_2 (1.000 g) were added to distilled water (50 mL) at room temperature. After stirring for 12 h in air, water was removed by rotary evaporation under reduced pressure to obtain the solid product. The obtained powder was dried at 110 °C for 5 h. After drying, the powder was calcined at 500 °C for 3 h under a static air atmosphere to obtain Pt/TiO_2 as a grey powder. As determined using ICP-AES, the Pt contents in Pt/TiO_2 was 5.56 wt%. The other catalysts were prepared in a similar way using various metal salts and supports. All catalysts were applied to the reaction without any pre-reduction step.

Typical reductive amination procedure (Table 1, entry 1)

The reductive ammonolysis of Poly(ε-caprolactone) (PCL) was carried out in a 50 mL stainless steel autoclave equipped with a Teflon vessel. The vessel was charged with PCL (57 mg, 0.5 mmol relative to the formula weight of constitutional repeating unit), Pt/TiO_2 (150 mg), and *n*-heptane (10.0 mL), and a Teflon-coated magnetic stir bar was added. The reactor was sealed, purged five times with 0.7 MPa NH_3, then pressurized with H_2 (4.0 MPa) and NH_3 (0.7 MPa), heated to 180 °C, and stirred at 900 rpm for 6 h. After the reaction, the autoclave was cooled in an ice-water bath, and reaction gas was released. The resulting reaction mixture was diluted with ethanol and analysed by GC-FID.

Product yields were calculated by the following equation:

$$yield\ (based\ on\ PCL) = \frac{amount\ of\ product\ (mmol)}{amount\ of\ loaded\ PCL\ (mmol)} \times 100 \qquad \text{(eq. S1)}$$

Catalyst reuse experiments (Figure 1)

After the reductive ammonolysis was complete, the catalyst was separated from the reaction mixture by centrifugation, washed with chloroform, ethanol, and then with *n*-hexane in air. The obtained powder was dried at 110 °C for 5 h and then calcined at 400 °C for 3 h before being reused in a subsequent reaction.

Pt/TiO_2 pre-reduction (Figure 2, S4, and S6)

Pt/TiO_2 was pre-reduced for the characterizations in Figure 2 and S1 under the typical reductive ammonolysis conditions without substrates: Pt/TiO_2 (150 mg), *n*-heptane (10.0 mL), 180 °C, H_2 (4.0 MPa), NH_3 (0.7 MPa), 2 h.

3. Supplementary tables

Table S1 Specific surface area (SSA) and the yields

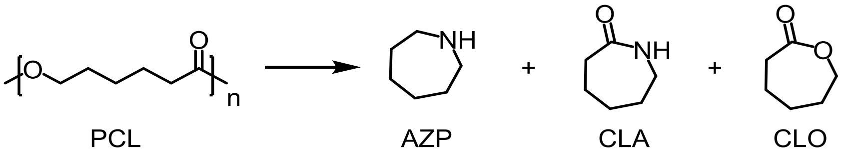

Entry	Catalyst	crystal type	SSA[a] [m^2/g]	Conversion[b] [%]	Yield[c] [%]		
					AZP	CLA	CLO
1	JRC-TIO-1	Anatase	72.6	>99	0	11	6
2	JRC-TIO-5	Rutile-anatase	2.6-2.7	59	0	0	11
3	JRC-TIO-9	Anatase	290-310	98	18	24	0
4	JRC-TIO-16	Rutile	109.5	>99	0	0	5
5	JRC-TIO-17	Anatase	50	>99	0	18	0
6[d]	JRC-TIO-9	Anatase	290-310	>99	75	0	0

[a] Specific surface are. The data were obtained from the Catalysis Society of Japan. [b] The conversions were obtained from the unreacted PCL weight. Reaction conditions: Pt/TiO_2 (150 mg, Pt: 8 mol%), substrate (0.5 mmol), *n*-heptane (10 mL), 180 °C, H_2 (4 MPa), NH_3 (0.7 MPa), 6 h. [c] The yields were determined using gas chromatography-flame ionization detection (GC-FID) with an internal standard. [d] Reaction time 25 h.

Table S2 ICP-AES analyses of Pt/TiO_2 before and after reaction

Sample	Amount (wt%)		Atomic ratio
	Pt	Ti	Pt/Ti
Fresh Pt/TiO_2	5.56	51.1	0.0267
Pt/TiO_2 after 1st run	5.69	51.2	0.0273
Pt/TiO_2 after 4th run	5.59	51.3	0.0267

Table S3 CHN analyses of Pt/TiO_2 before and after reaction

Sample Name	Amount [wt%]		
	C	H	N
Pt/TiO_2 fresh	0.09	0.36	0.05
Pt/TiO_2 after 1st run	0.30	0.22	0.03
Pt/TiO_2 after 1st run[a]	1.57	0.58	0.35
Pt/TiO_2 after 4th run	0.53	0.22	0.05

[a] After the 1st run, the catalyst was prepared by hexane washing and oven drying at 110 °C overnight, without any additional recovery/regeneration treatment.

Table S4 Control experiments

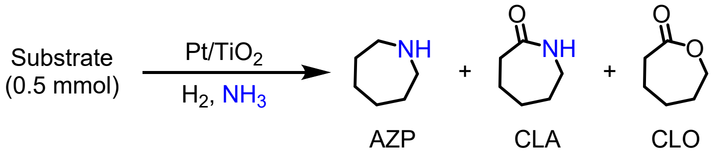

Entry[a]	Substrate	Conv. [%]	Yield[b] [%]		
			AZP	CLA	CLO
1	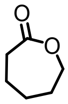 CLO	>99	25	24	-
2	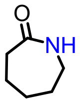 CLA	69	46	-	0
3	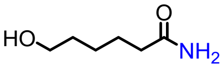 6-hydroxyhexanamide†	-	19	22	0
4	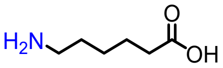 6-aminocaproic acid†	-	56	19	0

[a]Reaction conditions: Pt/TiO_2 (150 mg, Pt: 8 mol%), substrate (0.5 mmol), *n*-heptane (10 mL), 180 °C, H_2 (4 MPa), NH_3 (0.7 MPa), 6 h. (†) water soluble intermediate, undetectable under the present GC conditions (Conversion was not determined due to analytical limitations); [b]Yield was determined by GC-FID using an internal standard for analysis and calculated based on PCL.

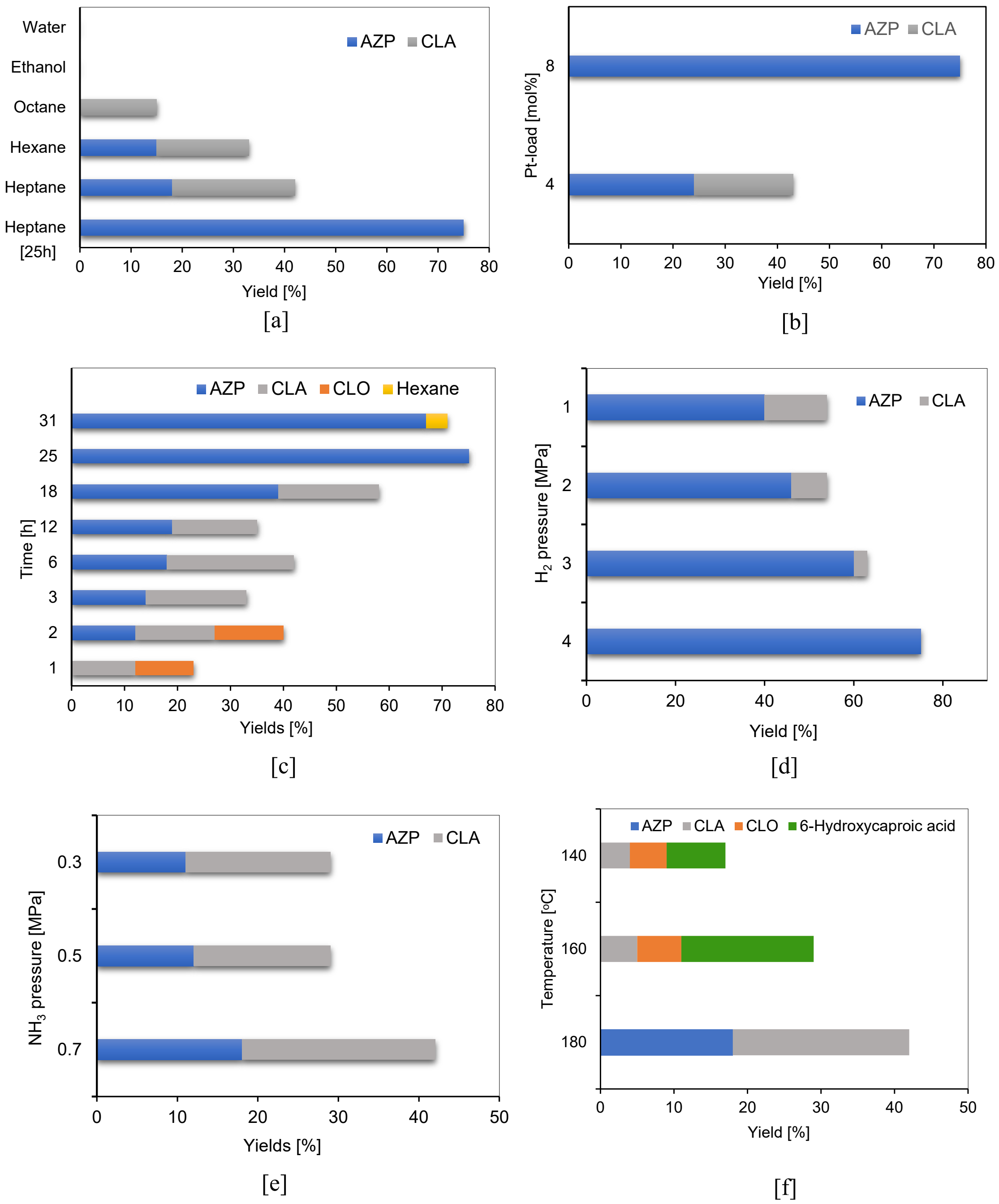

4. Supplementary figure

Figure S1 Condition screening for Pt/TiO_2-catalyzed reductive ammonolysis of PCL: (a) effect of solvent on product distribution (6 h), (b) effect of Pt loading (mol% per PCL repeat unit; 25 h), (c) product distribution at selected reaction times, (d) effect of H_2 pressure (25 h), (e) effect of NH_3 pressure (6 h), and (f) effect of reaction temperature (6 h). Yields were determined by GC–FID using an internal standard and are reported based on PCL repeat units.

Quantitative ^1H NMR analysis of the water-soluble fraction reveals transient formation of polar intermediates during the early stage of PCL reductive ammonolysis (Figure S2). The yields of 6-hydroxyhexanamide and 6-aminocaproic acid increase within the first 2 h and then decrease markedly at longer reaction times, consistent with their consumption as the reaction proceeds. In contrast, CLA becomes detectable after 2 h and is more prominent at extended reaction time, supporting its formation after the initial depolymerization/amination steps. These NMR results capture the time-dependent evolution of water-soluble intermediates and complement the product time-course in the organic phase discussed in the main manuscript (Figure 4). Several additional peaks are observed in the ^1H NMR spectra but cannot be assigned unambiguously. These signals are likely derived from oligomeric species formed during partial PCL depolymerization, which produce overlapping resonances in the aliphatic region.

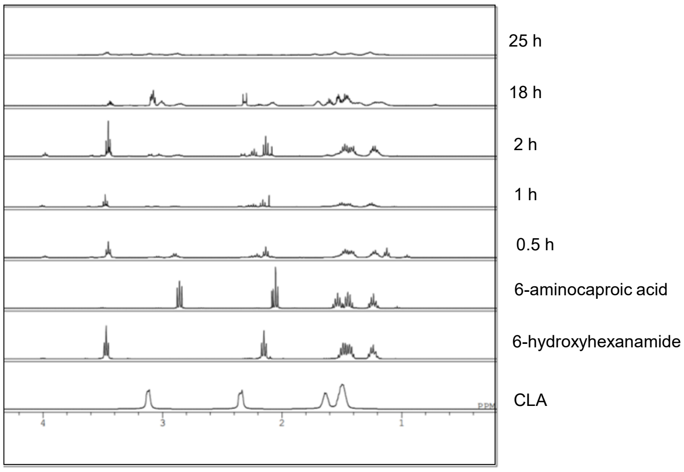

Reaction time[a]	Yield[b] [%]		
[h]	6-hydroxyhexanamide	6-Aminocaproic acid	CLA
0.5	10	7	0
1.0	23	14	0
2.0	32	19	4
18.0	3	4	18
25.0	5	3	5

[a]Reaction conditions: Pt/TiO_2 (150 mg, Pt: 8 mol%), PCL (0.5 mmol), *n*-heptane (10 mL), 180 °C, H_2 (4 MPa), NH_3 (0.7 MPa). ^1H-NMR analysis, the isolated solid products were dissolved in H_2O, the fraction was dried, and was measured in D_2O. [b]Yield was determined by ^1H-NMR integration using *s*-trioxane as internal standard.

Figure S2 ^{1}H-NMR spectra of CLA, 6-hydroxyhexanamide, 6-aminocaproic acid identification (reference standard), and the H_2O-soluble fraction obtained from the isolated solid products.

ε-Caprolactam (CLA): CAS registry No. [105-60-2]. ^{1}H-NMR (400 MHz, D_2O): δ/ppm 3.11-3.12 (m, 2H), 2.33-2.36 (m, 2H), 1.63-1.64 (m, 2H), 1.49-1.51 (m, 4H).

6-Hydroxyhexanamide: CAS registry No. [4547-52-8]. ^{1}H-NMR (400 MHz, D_2O): δ/ppm 3.49 (t, 2H, J = 6.4 Hz), 2.16 (t, 2H, J = 7.6 Hz), 1.40-1.55 (m, 4H), 1.24 (quint, 2H, J = 7.3 Hz).

6-Aminocaproic acid: CAS registry No. [60-32-2]. ^{1}H-NMR (400 MHz, D_2O): δ/ppm 2.86 (t, 2H, J = 7.6 Hz), 2.06 (t, 2H, J = 7.3 Hz), 1.56 (quint, 2H, J = 7.8 Hz), 1.45 (quint, 2H, J = 7.3 Hz), 1.24 (quint, 2H, J = 7.3 Hz).

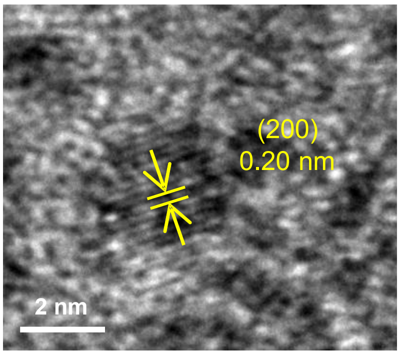

Figure S3 High-resolution TEM image of Pt/TiO_2 showing one-dimensional lattice fringes of the (200) lattice planes in Pt nanoparticles.

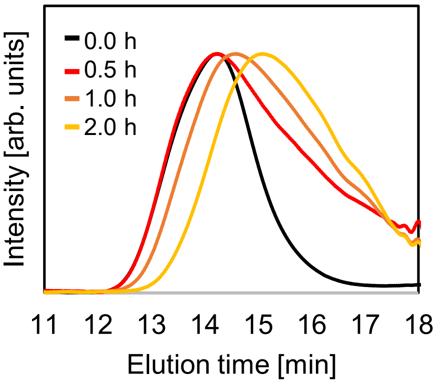

Reaction time [h]	*M*n [kg/mol]	*M*w [kg/mol]	Dispersity
0.0	20.1	26.7	1.3
0.5	6.4	18.3	2.8
1.0	6.3	14.9	2.4
2.0	5.6	11.4	2.0

Figure S4 GPC analysis of the residual PCL at different reaction times. Reaction conditions: Pt/TiO_2 (150 mg, Pt: 8 mol%), PCL (0.5 mmol), *n*-heptane (10 mL), 180 °C, H_2 (4 MPa), NH_3 (0.7 MPa).

XRD patterns (Cu Kα) of the reduced and after 4th run Pt/TiO_2 catalysts are dominated by TiO_2 reflections and show no additional crystalline phases, indicating that the TiO_2 crystallographic structure is preserved. Weak reflections assignable to metallic Pt (e.g., near 39–40°, consistent with Pt(111)) are discernible for both samples and are more pronounced after the 4th run (Figure S5). In addition, TEM corroborates nanoscale evolution of the Pt phase, with the mean particle size increasing from 2.7 ± 1.0 nm for reduced Pt/TiO_2 (n = 250) to 5.2 ± 1.2 nm in after 4th run, consistent with moderate sintering under the reaction conditions (Figure S5 and S6).

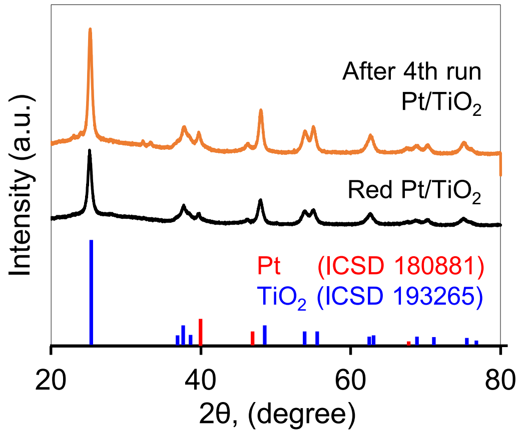

Figure S5 XRD pattern of reduced and after 4th run Pt/TiO_2.

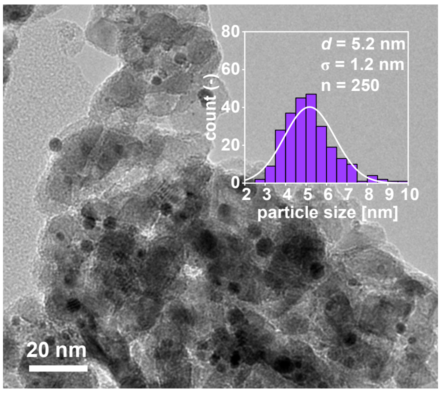

Figure S6 TEM image and size distribution histogram (inset) of Pt/TiO_2 after 4th run.

Curve fitting of the Pt 4f region reveals three Pt species assignable to Pt^{0}, Pt^{2+}, and Pt^{4+}.[1,2] Upon repeated use, the relative contribution of metallic Pt^{0} decreases from 0.77 for the fresh catalyst (Figure S7a) to 0.46 for the catalyst recovered after the 4th run (Figure S7b). This shift indicates a change in surface Pt speciation upon cycling.

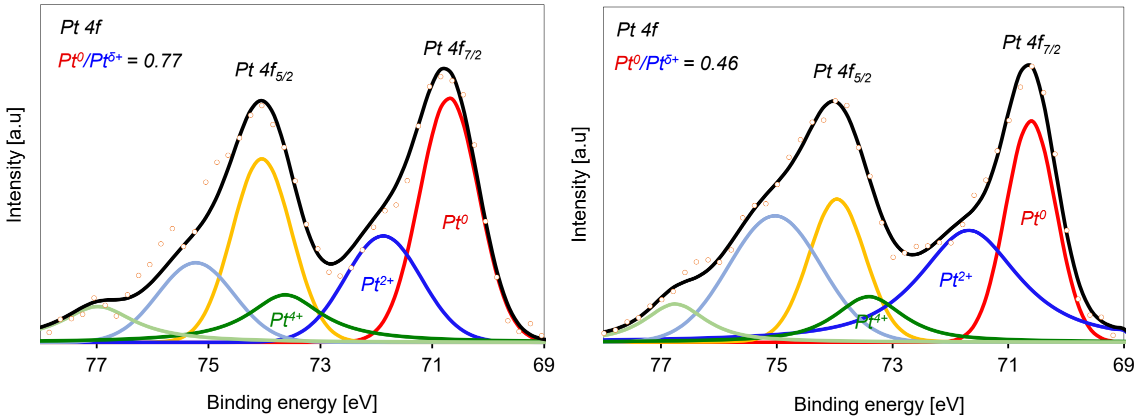

[a] [b]

Peak Position (eV)	Area	FWHM (eV)
PtTiO$_2$		
70.697	163.871	1.250
74.047	122.903	1.250
71.878	91.235	1.600
75.228	68.426	1.600
73.629	60.370	1.600
76.979	45.278	1.600
Pt/TiO$_2$ after 4th cycle		
70.604	173.212	1.020
73.954	129.909	1.150
71.666	243.569	2.050
75.016	182.677	1.880
73.390	71.601	1.400
76.740	53.701	1.250

Figure S7 Curve-fitted Pt 4f XPS spectra of Pt/TiO$_2$: (a) fresh catalyst and (b) after 4th run catalyst, showing the relative contributions of metallic Pt^{0} and oxidized Pt species (Pt^{2+} and Pt^{4+}).

Reduced Pt/TiO_2 exhibits the highest NH_3 desorption capacity (311 µmol g^{-1}) with both low- and high-temperature peaks, reflecting the coexistence of weak and strong acid sites (Figure S8a). In comparison, Pt/TiO_2 (141 µmol g^{-1}) and TiO_2 (115 µmol g^{-1}) show much lower acidity, indicating that reduction in the presence of Pt nanoparticles substantially strengthens surface acidity. This enhancement arises from the cooperation of Pt and TiO_2: Pt facilitates H_2 dissociation, and hydrogen spillover onto TiO_2 generates and stabilizes oxygen vacancies, which act as Lewis's acid sites.

The ESR spectra (Figure S8b) highlight how Pt and reduction modify TiO_2 defect states. Pristine TiO_2 (blue) shows a Ti^{3+} resonance at $g \approx 1.98$ and a weak vacancy signal at $g \approx 2.003$. After Pt deposition (red), the Ti^{3+} feature disappears due to electron transfer to Pt ($Pt^{\delta-}$ in XPS), while the vacancy signal intensifies and an O_2^- peak emerges at $g \approx 2.05$.[3] Upon H_2 reduction, Pt/TiO_2 (black) displays a dominant $g \approx 2.003$ resonance, confirming the generation of abundant F-centers by hydrogen spillover.[4] The persistence of vacancy signals and loss of Ti^{3+} together demonstrate that Pt deposition and reduction shift intrinsic Ti^{3+} defects toward stable vacancy-trapped electrons and O_2^- species, which underpin the stronger acidity observed in NH_3-TPD.

Taken together, the NH_3-TPD and ESR results demonstrate that reduced Pt/TiO_2 possesses both the highest density of acid sites and the largest population of surface oxygen vacancies. This dual enhancement provides a bifunctional environment, where electron-rich Pt nanoparticles and vacancy-stabilized acid sites cooperate to activate hydrogen, ammonia, and carbonyl groups. Such synergy explains the superior catalytic performance of reduced Pt/TiO_2 in PCL depolymerization to AZP.

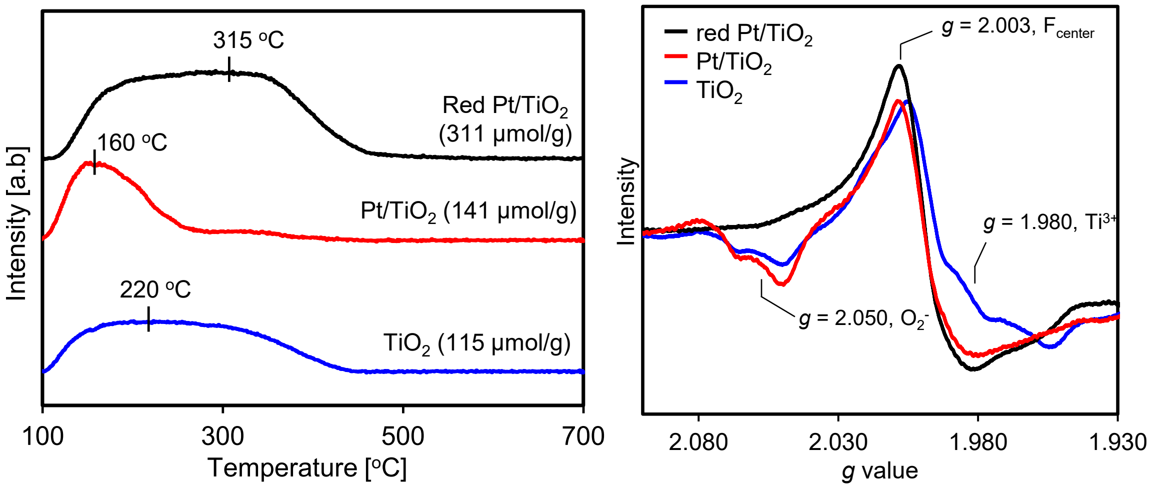

[a] [b]

Figure S8 [a] NH_3-TPD profiles of TiO_2, Pt/TiO_2, and reduced Pt/TiO_2, [b] ESR spectra of TiO_2, Pt/TiO_2, and reduced Pt/TiO_2.

To systematically examine the influence of oxygen vacancies, Pt/TiO_2 was pre-reduced under flowing H_2 at 200 °C for 2h and 6h prior to reaction. The ESR spectra (Figure S9) show that the defect signal at g ≈ 2.003, assigned to oxygen-vacancy-related sites, increases after H_2 pretreatment. For reference, we also show the ESR spectrum of Pt/TiO_2 exposed to the reaction atmosphere (H_2/NH_3, 180 °C, 2h) to indicate the *in-situ* vacancy level (black line). Consistent with the ESR trend, AZP formation increases significantly upon introducing H_2 pretreatment (18% → 48% from 0 h to 2 h). Importantly, extending the H_2 pretreatment to 6 h causes only a slight increase in the oxygen-vacancy signal, indicating that a similar vacancy level is reached under these conditions. This is consistent with the modest additional increase in AZP yield (48% → 54%) and the concurrent decrease in CLA (11% → 8%). Overall, these results support that oxygen-deficient TiO_2 promotes the PCL upcycling sequence toward AZP via cooperative interactions with Pt.

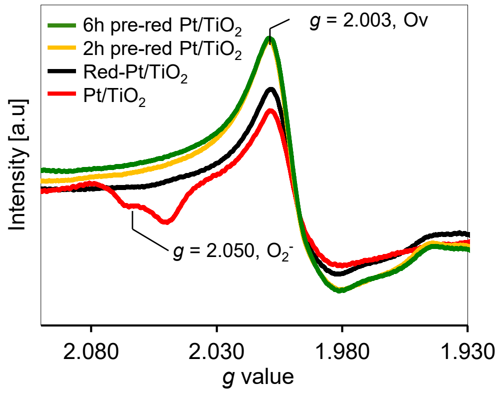

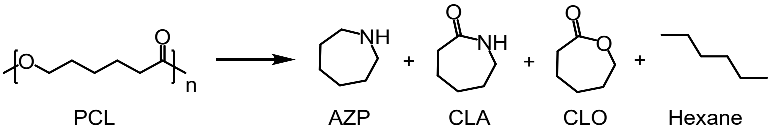

Entry[a]	Catalyst	Pre-reduction time [h]	Yield[b] [%]			
			AZP	CLA	CLO	Hexane
1	Pt/TiO_2 (red line)	0	18	24	0	0
2	Pt/TiO_2 (yellow line)	2	48	11	0	0
3	Pt/TiO_2 (green line)	6	54	8	0	3

[a] Pre-reduction condition: Pt/TiO_2 pre-reduced at 200 °C with H_2 flow 200 mL/minute. Reaction conditions: Pt/TiO_2 (150 mg, Pt: 8 mol%), PCL (0.5 mmol), *n*-heptane (10 mL), 180 °C, H_2 (4

MPa), NH_3 (0.7 MPa), 6 h. [b]Yield was determined by GC-FID using an internal standard for analysis and calculated based on PCL.

Figure S9 ESR spectra of Pt/TiO_2, reduced Pt/TiO_2 and pre-reduced Pt/TiO_2.

The *in-situ* FT-IR spectra of pyridine adsorption (Figure S10) further confirm the acidity enhancement in reduced Pt/TiO_2. Compared to TiO_2 and Pt/TiO_2, the reduced sample shows markedly stronger Lewis bands (~1530 and 1450 cm^{-1}) and the highest Lewis-to-Brønsted (L/B) ratio (1.7 vs. 1.5 for Pt/TiO_2). This increase in Lewis's acidity is consistent with the higher acidity measured by NH_3-TPD and the abundant oxygen vacancies identified by ESR (Figure S8a and S8b). The higher L/B ratio highlights stronger Lewis's acidity, which is crucial for carbonyl activation in PCL depolymerization. Together with ESR and NH_3-TPD results, the FT-IR data confirm that Pt–TiO_2 cooperation enriches vacancy-stabilized Lewis sites, providing the bifunctional surface environment required for selective PCL depolymerization to AZP.

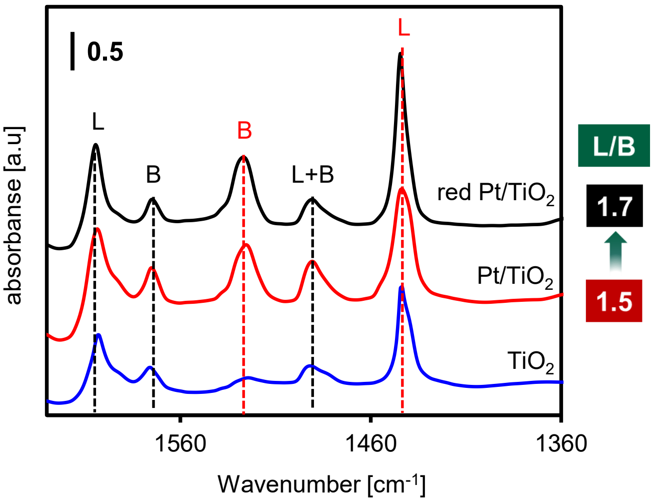

Figure S10 *In situ* FT-IR profiles of pyridine absorbed on TiO_2, Pt/TiO_2, and reduced Pt/TiO_2.

The CO_2-TPD profiles (Figure S11) clearly distinguish the basic properties of the catalysts. TiO_2 exhibits only weak CO_2 desorption with a total uptake of 40 µmol g^{-1}, reflecting a low density of surface basic sites. Pt/TiO_2 shows a slight increase to 54 µmol g^{-1}, indicating that Pt deposition alone does not substantially modify the basicity of TiO_2. In sharp contrast, reduced Pt/TiO_2 displays a significantly higher CO_2 uptake of 115 µmol g^{-1}, with two distinct desorption peaks centered at 158 °C and 340 °C confirming that reduction markedly enhances surface basicity. This increase originates from surface oxygen vacancies and adjacent Ti^{3+} species acting as Lewis's base centers that bind CO_2 through its carbon atom to form bent CO_2^- species, consistent with DFT and spectroscopic reports.[5–8]. The enhanced basic sites complement Lewis acidic Ti centers, creating a cooperative acid–base surface favorable for N–H activation during PCL depolymerization.

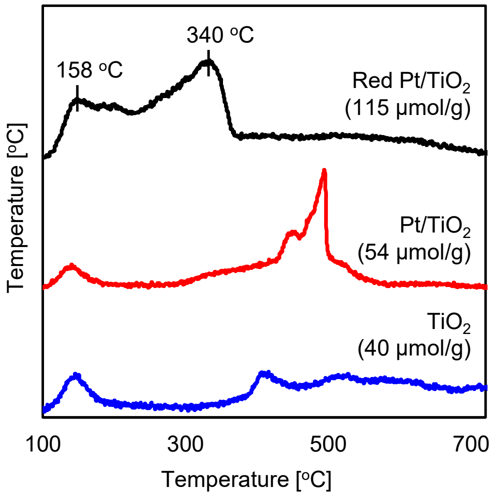

Figure S11 CO_2-TPD profiles of TiO_2, Pt/TiO_2, and reduced Pt/TiO_2.

In situ FT-IR spectra of acetone adsorption provide direct evidence of carbonyl activation on reduced Pt/TiO_2 (Figure S12a). The C=O stretching vibration shifts from 1736 cm^{-1} in the gas phase to 1696 cm^{-1} upon adsorption, indicating strong interaction with oxygen vacancies that function as Lewis's acid centers. Such activation of the C=O bond is a crucial step in the depolymerization of PCL intermediates. In situ FT-IR spectra of NH_3 adsorption on reduced Pt/TiO_2 (Figure S12b) show two absorption bands at 1594 and 1556 cm^{-1}, corresponding to NH_3 bound to surface base sites and to acid–base pair sites, respectively. The presence of acid–base pair sites is particularly significant, as they provide enhanced N–H activation compared with base sites alone.[9,10] Collectively, these results confirm the dual functionality of reduced Pt/TiO_2 (Figure 3): oxygen vacancies promote C=O activation, while acid–base pair sites facilitate N–H activation. This cooperative surface chemistry underpins the reductive ammonolysis pathway leading to the selective conversion of PCL to AZP.

[a]

[b]

Figure S12 [a] *In-situ* FT-IR profiles of acetone absorbed on reduced Pt/TiO_2 and acetone vapor. [b] *In-situ* FT-IR profiles of NH_3 gas absorbed on reduced Pt/TiO_2.

5. Green metrics (atomic economy and E-factor)

Atomic economy was calculated according to the definition proposed by Trost.[11] The environmental factor (E-factor) was estimated following the approach described by Sheldon.[12]

Atomic economy (AE)

For an idealized conversion of one PCL repeat unit to AZP, with water as the only stoichiometric by-product, the balanced equation is:

$$\text{PCL (repeat unit)} + NH_3 + 2\ H_2 \rightarrow \text{AZP} + 2\ H_2O$$

Using M_W (PCL repeat unit, $C_6H_{10}O_2$) = 114.14 g mol^{-1}, M_W (NH_3) = 17.03 g mol^{-1},
M_W (H_2) = 2.016 g mol^{-1}, and M_W (AZP, $C_6H_{13}N$) = 99.17 g mol−1, the atomic economy (EA) is:

$$\begin{aligned} AE &= M_W(AZP) / [M_W\ (PCL) + M_W\ (NH_3) + 2\times M_W\ (H_2)] \\ &= 99.17 / (114.14 + 17.03 + 4.03) \\ &= 0.733\ (73.35\%) \end{aligned}$$

E-factor (solvent-recovered scenario; AZP as the sole product).

The E-factor was calculated by considering AZP as the sole product and assuming solvent recovery; only stoichiometric water was counted as waste. Using the AZP yield of 75%:

$$\begin{aligned} E &= [2\times M_W\,(H_2O)] / [0.75\times M_W\ (AZP)] \\ &= 36.03 / (0.75\times 99.17) \\ &= 0.484\ (0.48) \end{aligned}$$

6. Catalyst reusability: performance evolution and post-reaction characterization

The catalyst recovered after the fourth run was characterized to assess how the active phase and surface chemistry evolve under repeated reductive ammonolysis conditions. AZP formation remained essentially unchanged over the first four runs. In the fifth run, however, AZP yield decreased while ε-caprolactam (CLA) remained detectable, consistent with a less effective hydrogenation stage upon extended use (Figure 1).

Post-reaction characterization indicates that this performance change reflects nanoscale and surface evolution rather than Pt loss. ICP-AES confirms that the Pt loading is retained from the catalyst prior to reaction to the catalyst recovered after the fourth run (5.56 vs 5.59 wt%), with a constant Pt/Ti atomic ratio (0.0267) (Table S2). Complementary XRD analysis was performed to assess the crystalline state. No new crystalline phases are observed after cycling, while weak Pt reflections near 39–40° (consistent with Pt(111)) become more discernible, indicating growth of crystalline Pt domains (Figure S5). Supporting this observation, TEM provides direct evidence for nanoscale evolution of the Pt phase upon repeated use, with the mean particle size increasing from 2.7 ± 1.0 nm before reaction to 5.2 ± 1.2 nm for the recovered catalyst, consistent with moderate sintering under the reaction conditions (Figure 2b and Figure S6).

Elemental analysis (CHN) further reveals pronounced carbon accumulation during repeated use. The carbon content increases from 0.09 wt% for the fresh catalyst to 0.53 wt% for the recovered catalyst (after 4th run), corresponding to an ~5.9-fold increase, whereas the nitrogen content remains low and nearly invariant (0.03–0.05 wt%) (Table S3). This trend is consistent with gradual carbonaceous deposition that may partially mask accessible surface sites upon extended use.

Surface-sensitive Pt 4f XPS provides additional insight into the evolution of the catalytically relevant surface Pt population. Curve-fitting of the Pt 4f region shows a reduced relative contribution of metallic Pt^0 after cycling, with the fitted $Pt^0/Pt^{\delta+}$ area ratio decreasing from 0.77 to 0.46 (Figure S7). This shift implies fewer surface Pt^0 ensembles for hydrogenation, consistent with CLA persistence and its limited further conversion to AZP in the fifth run.

Overall, the combined evidence indicates that the performance change at extended reuse arises from nanoscale and surface evolution—Pt particle growth, substantial carbon accumulation, and altered surface Pt speciation—rather than changes in the total Pt loading.

7. References

1. L. K. Ono, B. Yuan, H. Heinrich and B. R. Cuenya, *J. Phys. Chem. C*, 2010, **114**, 22119–22133.
2. E. I. Vovk, A. V. Kalinkin, M. Yu. Smirnov, I. O. Klembovskii and V. I. Bukhtiyarov, *J. Phys. Chem. C*, 2017, **121**, 17297–17304.
3. T. Berger, M. Sterrer, O. Diwald, E. Knözinger, D. Panayotov, T. L. Thompson and J. T. Yates, *J. Phys. Chem. B*, 2005, **109**, 6061–6068.
4. B. Liu, K. Zhang, S. Wei, Y. Zhang, G. Liu, L. Wu and J. Li, *Fuel*, 2024, **376**, 132693.
5. D. C. Sorescu, J. Lee, W. A. Al-Saidi and K. D. Jordan, *J. Chem. Phys.*, 2012, **137**, 074704.
6. S. Huygh, A. Bogaerts and E. C. Neyts, *J. Phys. Chem. C*, 2016, **120**, 21659–21669.
7. T. L. Thompson, O. Diwald and J. T. Yates, *J. Phys. Chem. B*, 2003, **107**, 11700–11704.
8. C. Di Valentin, G. Pacchioni and A. Selloni, *J. Phys. Chem. C*, 2009, **113**, 20543–20552.
9. T. Tsuda, H. Ishikawa, M. Sheng, M. Hirayama, S. Suganuma, R. Osuga, K. Nakajima, J. N. Kondo, S. Yamaguchi, T. Mizugaki and T. Mitsudome, *J. Am. Chem. Soc.*, 2025, **147**, 14326–14335.
10. A. A. Tsyganenko, D. V. Pozdnyakov and V. N. Filimonov, *J. Mol. Struct.*, 1975, **29**, 299–318.
11. B. M. Trost, *Science*, 1991, **254**, 1471–1477.
12. R. A. Sheldon, *Chem. Soc. Rev.*, 2012, **41**, 1437–1451.